Materials Advances

PAPER

View Article Online
View Journal | View Issue

Check for updates

Cite this: *Mater. Adv.*, 2021, 2, 4041

Graphitic carbon nitride embedded-Ag nanoparticle decorated-$ZnWO_4$ nanocomposite-based photoluminescence sensing of Hg^{2+}†

Uday Kumar Ghorui,[a] Jit Satra,[a] Papri Mondal,[a] Sourav Mardanya,[a] Arpita Sarkar,[a] Divesh N. Srivastava,[b] Bibhutosh Adhikary*[a] and Anup Mondal*[a]

Received 10th March 2021,
Accepted 28th April 2021

DOI: 10.1039/d1ma00211b

rsc.li/materials-advances

The adverse effects of the advancement of civilization have damaged the environment significantly by heavy metal ion toxicity, empoisoning soil, water, food, *etc.* In this work, Ag loaded metal tungstate–organic framework-based nanomaterials (g-C_3N_4/Ag/$ZnWO_4$) which can generate more and more oxygen defects have played a crucial role in detecting selective toxic metal ions in solution. The PL intensity of the samples increases with compositing $ZnWO_4$ with g-C_3N_4 and Ag, as the recombination of excited electrons with the holes at the oxygen vacancy sites increases. Here, a novel strategy has been adopted to develop a nanocomposite assembly of Ag-loaded $ZnWO_4$ nano-rods with π conjugated sp^2 hybridized g-C_3N_4 for fluorescence detection of Hg^{2+}. The prepared nanocomposites have displayed great fluorescence catalysis for Hg^{2+} sensing in terms of selectivity, sensitivity, activity, and reaction kinetics. A linear relationship in the range of 0 nM to 2 μM has been obtained for the detection of Hg^{2+} in a buffer solution of pH = 7.2 (phosphate buffer) by the fluorophore g-C_3N_4/Ag/$ZnWO_4$ and the minimum detection limit was found to be 0.23 nM. Furthermore, the synthesized nanocomposites were applied for Hg^{2+} detection in few real samples (pond water, sewage water, *etc.*), signifying their potential application in routine Hg^{2+} analysis. The probable mechanistic pathway for the sensing of Hg^{2+} by grafting the metal ion has also been studied in detail. Based on this mechanism an electronic computing system using an Implication circuit device has been constructed from the molecular information processing and a probable fluorescence mechanism (Jablonski diagram) was explored in which the material was found to possess some room-temperature phosphorescence (RTP).

Introduction

Extensive contamination of water, soil, food, *etc.* by toxic heavy metal ions is a global environmental concern.[1,2] With the advancement of civilization, industrial activities have increased rapidly which has affected biodiversity through the entry of toxic metal ions into the environment. It is well known that heavy metals such as Hg, Pb, As, Cd, *etc.* are very toxic and carcinogenic, even at trace levels.[3,4] They are non-biodegradable and can be stored in the food chain and drinking water, carrying a severe threat to living species. Among these toxic metals, all the three oxidation states of mercury (0, +1, and +2) are extremely harmful. Moreover, Hg^{2+} is highly soluble in water.[5,6] The ever-increasing uses of batteries, pesticides, paper, fluorescent lamps, *etc.* in developing countries are the main cause of the growing possibilities of mercury exposure to humans and animals and are mainly responsible for Hg^{2+}contamination in the environment. Again, organo-mercury compounds such as methyl mercury (MeHg), phenyl mercury (PhHg), and ethyl

---

[a] *Department of Chemistry, Indian Institute of Engineering Science and Technology, Shibpur, Howrah-711103, West Bengal, India. E-mail: bibhutosh@chem.iiests.ac.in, bibhutoshadhikary@gmail.com, anupmondal2000@yahoo.co.in, anup@chem.iiests.ac.in; Fax: +91-033-2668-2916; Tel: +91 8902524532, +91 9681420714, +91-033-2668-4561-64 ext. 512*

[b] *Department of Analytical Science, Central Salt and Marine Chemicals Research Institute, Gijubhai, Badheka Marg, Bhavnagar 364002, Gujarat, India*

† Electronic supplementary information (ESI) available: Materials, synthesis of the g-C_3N_4/Ag/$ZnWO_4$ nanocomposite, sample characterization, FESEM, EDX and table of EDX results, BET and table of BET results with ICP data, quantum yield calculation plot and table, fluorescence lifetime comparison table, PL emission plot of g-C_3N_4/Ag/$ZnWO_4$ with other metal ions, fluorescent quantitative detection of Hg^{2+}, Stern–Volmer plot, fluorescence lifetime, comparison table for fluorescence lifetime, discussion of lifetime, PL spectra of different pH and the corresponding histogram, overall XPS scan for the g-C_3N_4/Ag/$ZnWO_4$ nanocomposite after the addition of Hg(II) salt, UV-Vis pH effect and quantitative plot, PL emission spectra at different excitation wavelengths, time resolved fluorescence stability, fluorescence excitation and emission spectra with the phosphorescence emission spectrum, binding constant and binding site calculation, Jablonski diagram for the PL mechanism with PL emission, excitation and phosphorescence plot, recyclability test and verification of morphology (TEM image and FESEM image) and composition (EDX) for nanocomposites, and a comparison table for Hg^{2+} sensing efficiency. See DOI: 10.1039/d1ma00211b

mercury (EtHg) have high toxicity due to their high biomagnification factor (up to 10^6) and lipo-solubility in drinking water and the food chain.[7] The inorganic mercury species can also be converted into organo-mercury species by microalgae and microorganisms present in the aquatic ecosystem.[8] The various forms of Hg can readily be absorbed through direct skin contact and the respiratory system and can easily cross the blood–brain barrier.[9] High-level exposure to mercury can cause damage to human health and lead to Minamata disease, various Acrodynia diseases and system failure.[9–13] According to WHO standard guidelines the maximum Hg^{2+} tolerance is 10 nM in food and drinking water.[14] So, heavy metal ion pollution is a grave concern in global sustainability. It is, therefore, essential to detect mercury so that it can be properly disposed of from the environment.

At present, considerable efforts have been put forth for the detection and removal of various toxic metal ions by applying different nanomaterials, using colorimetric and fluorimetric techniques.[15–18] Therefore, developing a highly sensitive and selective technique for the detection of trace amounts of a toxic metal ion such as Hg^{2+} has become a topic of major research interest. Several techniques have been established for the detection of toxic metal ions like Auger-electron spectroscopy, atomic absorption/emission spectroscopy (AAS/AES), polarography, inductively coupled plasma mass spectrometry (ICP-MS), *etc.* However, these instrumental techniques are quite sophisticated and generally complicated, costly, time consuming, and require intricate sample preparation, which brings limitations to their practical applications.[19–21] Recently, nanomaterial-based fluorimetric assays have been widely used to detect Hg^{2+} in solution for quick analysis as the method is cost effective, ultra-sensitive, and selective, but is a less cell-damaging technique in which the transformation of color would be readily perceived by the naked eye even at very low concentration of the analyte.[22] Among the various types of metal oxides, metal tungstates such as $ZnWO_4$, $CdWO_4$, $PbWO_4$, Bi_2WO_6, *etc.* have achieved considerable attention due to their unique physicochemical properties and simplistic synthetic routes.[23,24] Most of the tungsten-based metal oxides are found to be inactive in fluorescence. Meanwhile, several recent studies have shown that the transition metal oxides with d^0 and d^{10} configurations are more catalytically active under light irradiation.[25] Furthermore, it has been observed that wolframite $ZnWO_4$ with the $d^{10}s^2$–d^0 electronic configuration[26] has greater catalytic activity than that of other metal tungstates $M^{II}WO_4$ (M^{II} = Co, Ni, Cu, Pb, Cd and Ca).[27,28] Huan-Tsung Chang *et al.* revealed that metallic nanoparticles (NPs) like Au, Ag, *etc.* which are used for the detection of toxic metal ions by ICP-MS are encapsulated with a very costly polymeric moiety,[29] which is expensive and not suitable for on-site analysis. Loading of noble metals[30,31] (*e.g.* Ag, Au, Pd, Pt, *etc.*) with a metal oxide or organic polymer has aroused keen interest in the field of biosensing as they exhibit size-dependent Surface Plasmon Resonance (SPR) with intense color. The presence of a special arrangement of a delocalized π conjugated single atomic layer of sp^2 hybridized carbon (and nitrogen also, in some cases) in g-C_3N_4, reduced graphene oxide (RGO),[32] PANI,[33] C_{60}, *etc.*, has created a vast impact on their biosensor applications.[34–36] Compared to graphene, g-C_3N_4 has a unique structure of tri-*s*-triazine units, linked by an amino group with periodic lattice vacancies that can lead to the tuning of its optical properties.[37] Therefore, noble metal (Ag) loaded $ZnWO_4$ composited with g-C_3N_4 can attract extensive scientific interest towards fluorescence and electrochemiluminescence sensing of toxic metal ions.[38,39] We intend to fabricate a device that can act as an ultrasensitive stable biosensor by grafting Hg^{2+} ions in an aqueous solution. Owing to the tunable fluorescence properties of Ag NPs, a composite (g-C_3N_4/Ag/$ZnWO_4$) has been synthesized and demonstrated to work as a ''turn off'' probe in an aqueous solution that can quench the photoluminescence (PL) intensity in the presence of toxic metal ions like Hg^{2+}. Moreover, the capability of the molecules to process molecular information identical to electronic systems was already demonstrated by de Silva *et al.*, but it is still a significant challenge to construct molecular information technology-based memory devices.[40,41] Developing a molecular computing system based on the response profile towards Hg^{2+} detection in terms of emission intensities at the emission wavelength that can mimic advance Boolean logic functions like OR, XOR, NOR, AND, *etc.* would be a significant achievement.

In this present work, we present a newly designed material that has not only displayed a better luminescence property due to sufficient oxygen vacancies but also proved to be a cost-effective, ultrasensitive and rapid ''turn off''–''turn on'' fluorescent biosensor. A facile synthetic route has been constructed to prepare a fluorescent g-C_3N_4/Ag/$ZnWO_4$ heterojunction which detects the highly toxic Hg^{2+} ion selectively in a buffer solution of pH = 7.2. Also, a possible static quenching mechanism for the catalytic effect of Hg^{2+} detection by the heterostructure has been established based on trapping/grafting of Hg^{2+} with the N atom of g-C_3N_4. Furthermore, a response profile in terms of emission intensities and wavelength towards Hg^{2+} ions has been constructed using the binary logic function (implication logic gate) for the development of molecular computing.

Experimental details

Synthesis of nanocomposites

The syntheses of Ag NPs[42] and the nanocomposites were performed as per literature methods [mentioned in the ESI†][43] and have been shown schematically in Scheme 1.

PL sensing of Hg^{2+} ions

A stock solution of 1 mg mL^{-1} of g-C_3N_4/Ag/$ZnWO_4$ was prepared by dispersing 50 mg of solid g-C_3N_4/Ag/$ZnWO_4$ in 50 mL of Mili-Q water. 10 μL of g-C_3N_4/Ag/$ZnWO_4$ stock solution was diluted with 2 mL water to perform the PL quenching experiment and different concentrations of 2 μL Hg^{2+} solutions were added, keeping the mixture under static conditions for 2 min to attain equilibrium. The resultant concentration of the Hg^{2+} was 100 times less than the initially added Hg^{2+}. After 2 min, the PLs of the mixture solutions with different amounts of Hg^{2+} were recorded with an excitation wavelength 310 nm at

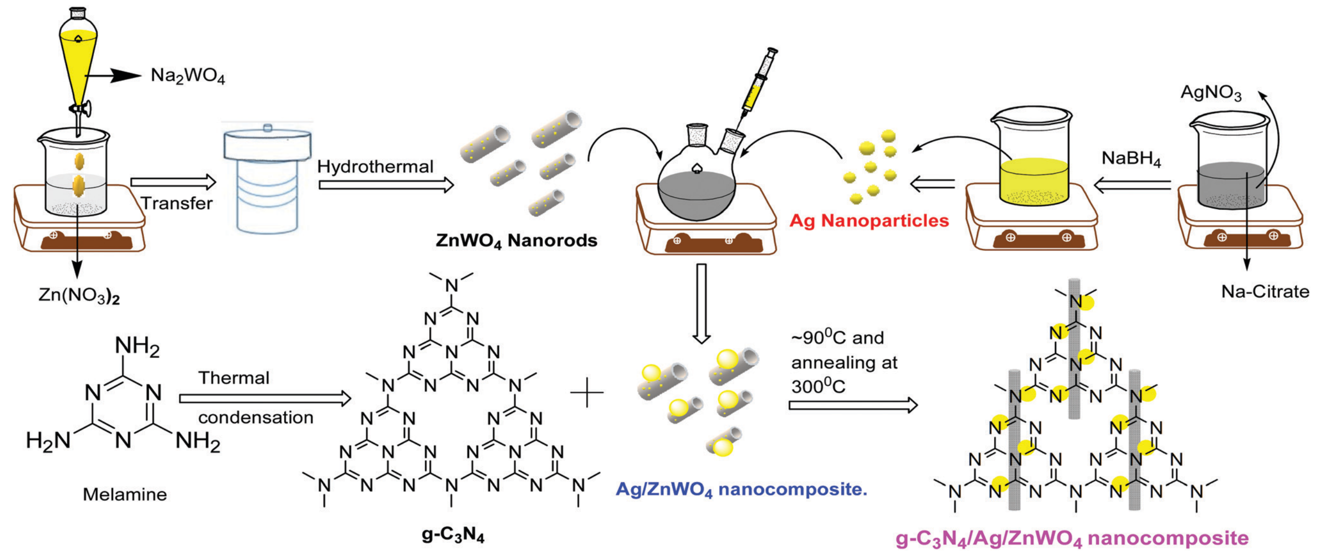

Scheme 1 Proposed synthetic scheme to prepare g-C_3N_4/Ag/$ZnWO_4$ nanocomposites.

room temperature. The selectivity of g-C_3N_4/Ag/$ZnWO_4$ towards Hg^{2+} was compared with other metal ions such as Fe^{3+}, Cd^{2+}, Cu^{2+}, K^{+}, Mn^{2+}, Ni^{2+}, Ca^{2+}, Pb^{2+} and Co^{2+} under identical conditions. The concentration of the various metal ions used for the PL study was taken as 10 μM. Also, the detection sensitivity of Hg^{2+} in a mixture of several metal ions was determined.

Time resolved fluorescence stability test

The time resolved fluorescence stability test was performed in a solution medium of g-C_3N_4/Ag/$ZnWO_4$ at pH = 7.2 for 10 min. The excitation wavelength was 310 nm.

Quantum yield (QY) determination

The PL QY for the NPs were measured using 2-aminopyridine (2-AMP) in 0.1 (M) H_2SO_4 (Φ = 0.58) as a standard reference. Their integrated fluorescence intensities resulting due to excitation at 310 nm were compared using the following equation:

$$\Phi_X = \Phi_{ST} \times (G_X/G_{ST}) \times (\eta_X{}^2/\eta_{ST}{}^2)$$

where, Φ is the QY, G is the gradient of the plot, η is the refractive index of the solvent, x refers to pure and composited $ZnWO_4$ and ST refers to a standard reference (refractive index 1.58). A fixed concentration of 0.05 mg mL^{-1} (w/v) of the nanoparticles and the standard reference 2-AMP were so prepared that the absorbance of the solutions was less than 0.1 at their respective excitation wavelengths. The maximum quantum yield was found to be 11.40% for g-C_3N_4/Ag/$ZnWO_4$ (Fig. S4(A) and Table S2, ESI†). The refractive index of the phosphate buffer (pH = 7.2) used as a solvent was the same as that of water (1.335). This is because it does not absorb (*i.e.* absorption coefficient is zero) the usual laser wavelengths used in PL measurements.

Results and discussion

Material characterization

Based on our experimental findings, a synthetic scheme for the preparation of g-C_3N_4/Ag/$ZnWO_4$ has been proposed in Scheme 1. The basic structural unit consisting of three tri-*s*-triazine in g-C_3N_4 was prepared from melamine which can form a two-dimensional repeating network. It was then reacted with Ag/$ZnWO_4$ nanorods forming the composite which was characterized by X-ray diffraction (XRD), X-ray photoelectron spectroscopy (XPS), Transmission Electron Microscopy (TEM), High-Resolution TEM (HR-TEM) imaging, selected area electron diffraction (SAED) patterns, Field Emission Scanning Electron Microscopy (FE-SEM), Energy Dispersive X-ray (EDX), Brunauer–Emmett–Teller (BET) and UV-Vis spectroscopy. The optical properties of the as-synthesized NPs were analyzed (Fig. 1A and B) by dispersing the samples in Mili-Q water. From Fig. 1A, fundamental sharp absorption band edges are observed for both $ZnWO_4$ nanorods and g-C_3N_4 at 370 nm and 460 nm, respectively.[44,45] It was detected that after loading different amounts of g-C_3N_4 to the $ZnWO_4$ nanorods the absorption edges were red shifted from the UV to the visible region. This trend indicated the formation of heterojunction nanocomposites depicting a correlation between the graphitic carbon nitride content and the absorption intensity.[46,47] The UV-Vis absorption of the samples also increased with increasing g-C_3N_4 content. This suggests an increased electric surface charge on the oxide within the composite due to the introduction of g-C_3N_4. The introduction of g-C_3N_4 content might lead to higher electron shuttling for the detection of Hg^{2+}.[42] Fig. 1B demonstrates an absorption peak around 397 nm for pure Ag NPs (black line) due to size-dependent SPR[47] as the electrons can collectively oscillate in the metallic Ag NPs that can be excited by the light. However, a blue shift of 14 nm in the SPR band could be observed for the composite material, which might be due to the interaction between the conduction electrons of the Ag NPs

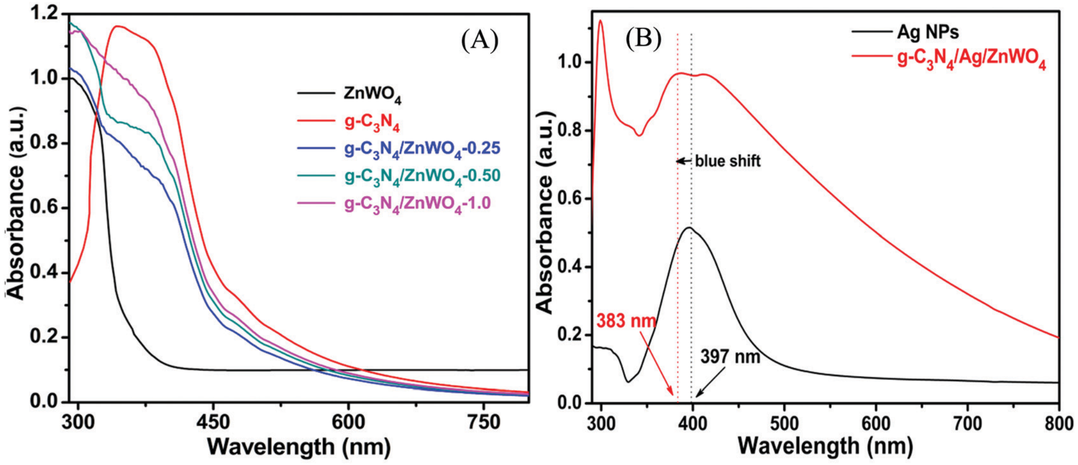

Fig. 1 (A) UV-Vis spectra of $ZnWO_4$, $g\text{-}C_3N_4$, and the $g\text{-}C_3N_4$ composite $ZnWO_4$. (B) UV-Vis spectra of pure Ag NPs and the Ag modified $g\text{-}C_3N_4/ZnWO_4$ composite.

at the interface and the sp^2 hybridized C atom in $g\text{-}C_3N_4$. The existence of this SPR band at a lower wavelength for the composite material (red line) can likely be associated with the formation of $g\text{-}C_3N_4$ embedded Ag NP decorated $ZnWO_4$ nanocomposites. Additionally, the broad background absorption intensity in the almost entire visible region for the nanocomposites, as shown in Fig. 1B, was enhanced with the incorporation of $g\text{-}C_3N_4$ into $Ag/ZnWO_4$, which might be attributed to the superior light absorption.[45] The peak at 306 nm indicated the presence of an *s*-triazine ring, which can be assigned to $\pi\text{–}\pi^*$ electronic transition while the $\sim$420 nm peak indicated $n\text{–}\pi^*$ transition due to the presence of a heteroatom in *s*-triazine. These results infer that the constructive effects in $g\text{-}C_3N_4/Ag/ZnWO_4$ promote higher electron shuttling which can be further confirmed by PL spectroscopy.

Fig. 2 represents the powder XRD patterns of various combinations leading to the formation of $g\text{-}C_3N_4/Ag/ZnWO_4$ nanorod composites. $Ag/ZnWO_4$ was prepared by introducing Ag nano-colloids in a suspension of $ZnWO_4$ nanorods in an aqueous medium for the growth of the nanocomposite. It is clear that the $ZnWO_4$ nanorods were of monoclinic primitive phase (JCPDS: 73-0554) (Fig. 2A) with an average crystallite size of 31.435 nm, derived using the Scherrer equation ($d = (0.9 \times \lambda)/(\beta\cos\theta)$). For $ZnWO_4$ nanorods the peaks at 19.10°, 24.00°, 24.75°, 30.62°, 36.63°, 41.40°, and 53.90° were indexed as the (100), (011), (110), (111), (021), (210) and (202) diffraction planes, respectively, of the pure monoclinic phase.

The peak at 2θ = 27.72° is for calcined $g\text{-}C_3N_4$ and it was slightly shifted by 0.2° in comparison to other reports, suggesting the characteristic interlayer stacking of aromatic systems.[48] The strong interaction of $g\text{-}C_3N_4$ with $ZnWO_4$ nanorods can be assigned to the appearance of the (002) plane at 27.5° (JCPDS: 87-1526) with an interlayer spacing of 0.324 nm for all the $g\text{-}C_3N_4$ nanocomposites, as shown in Fig. 2B. The absence of the (100) plane at 2θ = 13.1° in the nanocomposites was likely due to rapid growth and thinner sheet formation of $g\text{-}C_3N_4$ causing lattice distortion, which might lead to a decrease in crystal plane spacing.[49] Fig. 2B shows the effect of the addition of various amounts of $g\text{-}C_3N_4$ to $ZnWO_4$ nanorods. It can be concluded (from the inset image) that the maximum interfacial wall interaction was for 50% $g\text{-}C_3N_4$ w.r.t. $ZnWO_4$. This is possibly because

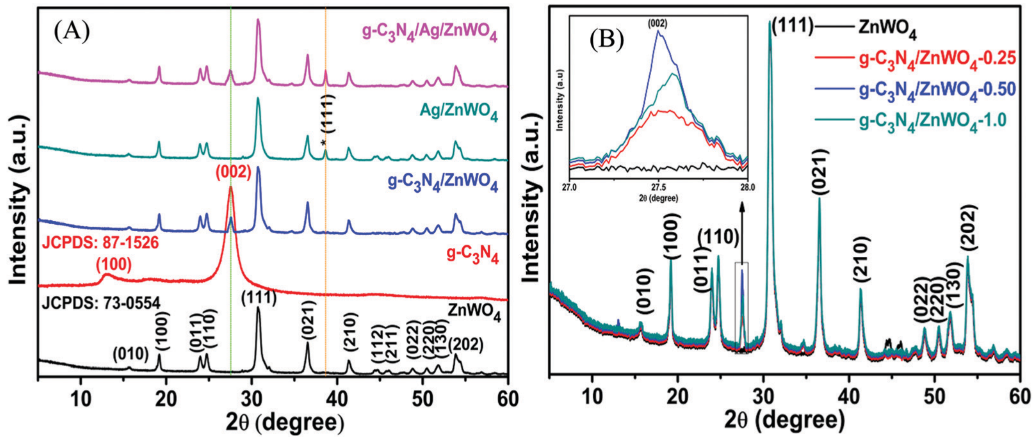

Fig. 2 Powder XRD of (A) pure monoclinic primitive $ZnWO_4$ and the composites of $ZnWO_4$ with $g\text{-}C_3N_4$ and Ag(0) and (B) composites with varying amounts of $g\text{-}C_3N_4$.

of the creation of more and more oxygen defects. The peak that appeared at 38.63° (Fig. 2A * marked) is the most intense peak for the (111) plane of silver (JCPDS: 03-0931) which denotes the formation of Ag NPs on the surface of $ZnWO_4$ nanocrystals and also on g-C_3N_4/$ZnWO_4$ nanocomposites.

To get a better perception of the formation and the morphology of $ZnWO_4$ NPs and the modified $ZnWO_4$ nanohybrid, TEM and HR-TEM analyses of them were carried out and presented in Fig. 3. Fig. 3A represents irregular hexagonal 'rod-shaped' $ZnWO_4$ NPs while, for the hybrid material (Fig. 3D) 'square-shaped plates' were found to develop, which are consistent with the FE-SEM image (Fig. S2B) shown in the ESI.† The length of the $ZnWO_4$ nano-rods is varied from 20 to 50 nm and the width is about 10–15 nm. Fig. 3B and E show clear lattice fringe patterns of $ZnWO_4$ nano-rods and the $ZnWO_4$ hybrid, respectively. The interplanar distance (*d*-spacing) in $ZnWO_4$ nano-rods is consistent with the (111) plane of the monoclinic primitive structure. On the other hand, for the hybrid material (g-C_3N_4/Ag/$ZnWO_4$) the *d*-spacing of 0.321 nm was obtained for the (002) plane of g-C_3N_4 at the edge of the $ZnWO_4$ nano-rods (Fig. 3E), along with $ZnWO_4$ and Ag(0) for their (011) and (111) planes, respectively. The SAED patterns are shown in Fig. 3C and F. The patterns seem to be concentric showing diffraction planes of (021), (011), and (100) for $ZnWO_4$ (Fig. 3C), and similarly, in Fig. 3F the planes (022) and (011) revealed the presence of $ZnWO_4$ in the nanocomposite g-C_3N_4/Ag/$ZnWO_4$, and the presence of the (111) plane for Ag(0) indicates the formation of the composite. These planes were consistent with the *d*-spacing values obtained from the XRD patterns mentioned earlier.

In context of the interaction of Ag with $ZnWO_4$, we have studied the UV-Vis spectroscopy of Ag/$ZnWO_4$ (Fig. S1A, ESI†). A shoulder is observed at around 380 nm which is due to the SPR band of Ag NPs as the characteristic peak for $ZnWO_4$ developed at 306 nm. Generally, the SPR band for Ag arises at around 400 nm or above. Therefore, a blue shift of the SPR band is noticed. The reason for this shift is mainly due to the confinement of energy levels of the electrons of Ag which is also supported by the TEM image (Fig. S1B, ESI†) and SAED pattern (Fig. S1C, ESI†) of Ag/$ZnWO_4$. The average length and width of the $ZnWO_4$ NPs decrease to 32 nm and 11 nm, respectively due to the incorporation of Ag. This confinement effect could lead to the synergistic behavior between the conduction electrons of Ag and $ZnWO_4$.[50] Further evidence of composite formation has also been demonstrated through EDX (Fig. S1D, ESI†) studies.

To obtain a better understanding of the shape and the elemental distribution in $ZnWO_4$ and g-C_3N_4/Ag/$ZnWO_4$ nanocomposites, FE-SEM and EDX analyses were performed. From Fig. S2A (ESI†) it can be confirmed that the $ZnWO_4$ nanomaterials possess a 'rod' shaped nanostructure while that of the g-C_3N_4/Ag/$ZnWO_4$ nanocomposite revealed a 'plate' like shape (Fig. S2B, ESI†). The typical EDX patterns (Fig. S2C and D, ESI†) indicate 1 : 1 : 4 atomic ratios of Zn, W, and O respectively.

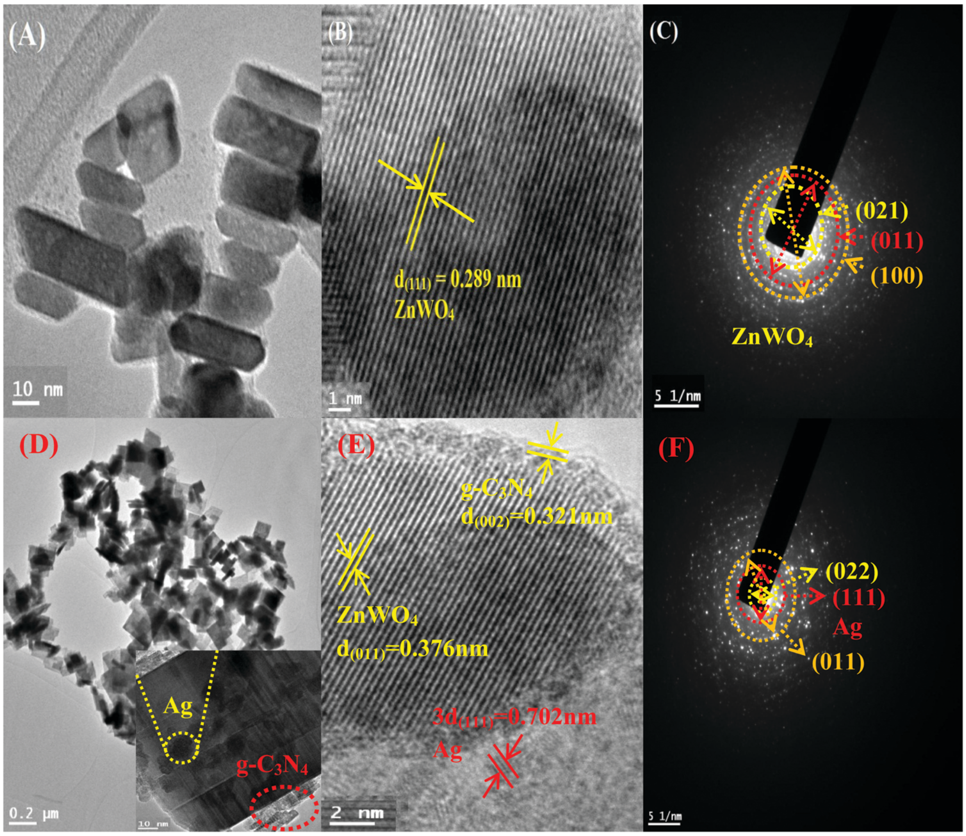

Fig. 3 (A)–(C) Show the TEM, HR-TEM, and SAED patterns of $ZnWO_4$, respectively, and (D)–(F) are TEM, HR-TEM, and SAED patterns of g-C_3N_4/Ag/$ZnWO_4$, respectively.

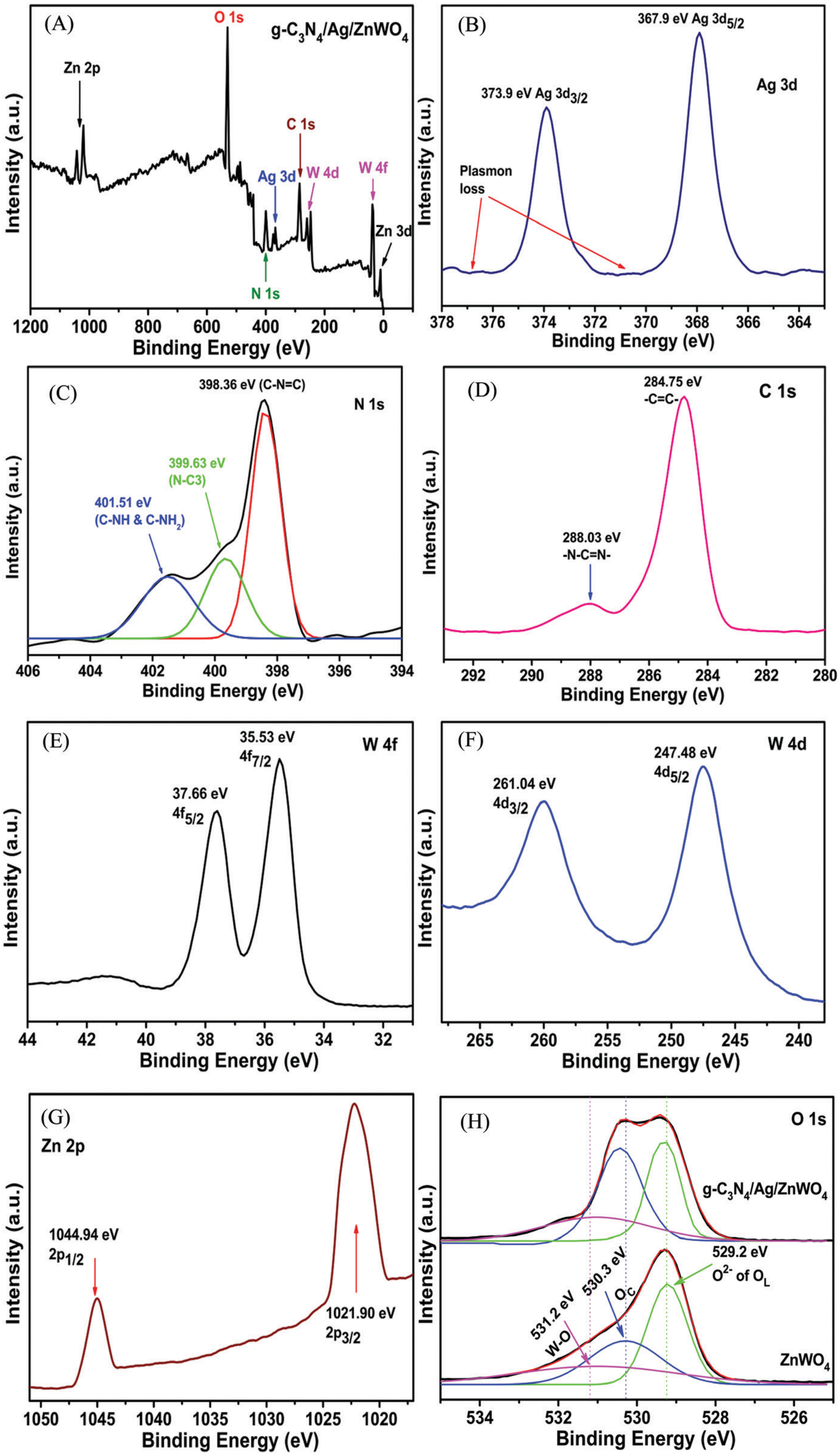

Fig. 4 (A) Overall XPS spectrum of g-C_3N_4/Ag/$ZnWO_4$ and the high-resolution XPS spectra (B) of Ag 3d, (C) of N 1s, (D) of C 1s, (E) of W 4f, (F) of W 4d, (G) of Zn 2p and (H) of O 1s.

The overall XPS (Fig. 4A) was investigated to establish the detail of the chemical composition of the as-prepared g-C_3N_4/Ag/$ZnWO_4$ nano-composites. A detailed survey of the Ag 3d peak near 380 eV of binding energy (BE) (Fig. 4A) was scrutinized in Fig. 4B, from which Plasmon loss is evidenced. Also, a comparably weak signal of the Ag 3d peak endorsed that Ag(0) is allied with the $ZnWO_4$ nano-rods. The peaks at 367.9 and 373.9 eV (Fig. 4B) are ascribed to Ag $3d_{5/2}$ and $3d_{3/2}$, respectively.[51,52]

However, a slight shift of the peak positions toward higher BE (concerning that of the pure Ag NPs) due to decreased Ag NP dimensions is also observed.[53,54] Depending on core–hole screening by conduction electrons (higher quantum confinement effects for lower size),[55] the peak position varies with the size of NPs.[52] From the XPS of the N 1s region (Fig. 4C), sp^2 hybridized nitrogen in C–N═C (398.36 eV), tertiary nitrogen N–(C)$_3$ (399.63 eV) and C–NH$_2$ and C–NH (401.51 eV), respectively could be endoresd.[52]

The presence of major carbon species in g-C_3N_4 (related to N–C═N groups of triazine rings) has been confirmed by the high-resolution C 1s spectrum (Fig. 4D) at higher BE; whereas, the peak centered at 284.75 eV originated due to sp^2 C═C bonds.[56,57] In a similar manner, the high-resolution spectra of W 4f and 4d (Fig. 4E and F, respectively) suggest that the tungsten metal is in +6 formal valence. Also, a formal valence of +2 for Zn is inferred from the detailed survey of Zn 2p peaks (Fig. 4G).[43,58] The presence of oxygen vacancies can be confirmed from the XPS spectra of O 1s for $ZnWO_4$ and g-C_3N_4/Ag/$ZnWO_4$ which have been fitted into three peaks, (1) at 529.2 eV for lattice oxygen (O_L), (2) at 530.3 eV for chemisorbed oxygen (O_C) and (3) at 531.2 eV for W–O bond.[59,60] Ye *et al.*[61] have reported that O_C designates the presence of oxygen vacancies and they established that the sample with a higher content of oxygen vacancies displayed a lower O_L/O_T ratio ($O_T = O_L + O_C + W - O$). In this study, the ratio of O_L to O_T is 0.59 and 0.42 for $ZnWO_4$ and g-C_3N_4/Ag/$ZnWO_4$, respectively. Thus, the composite has a higher concentration of oxygen vacancies than that of pure $ZnWO_4$.

To verify the assumption of an expanded surface area for the nanocomposite, the surface area of the photocatalysts was studied through BET analysis. Fig. S3 (ESI†) represents the nitrogen adsorption–desorption isotherms for the photocatalysts. The $ZnWO_4$ nano-rods exhibit a BET surface area of 29.2 $m^2\ g^{-1}$ whereas the composite g-C_3N_4/Ag/$ZnWO_4$ shows a relatively higher surface area of 55.7 $m^2\ g^{-1}$ (tabulated in Table S1, ESI†). The greater surface area of the nanohybrid composite could be ascribed to the unique architecture of the coated g-C_3N_4 on the surface of Ag/$ZnWO_4$. This result indicates that g-C_3N_4 can effectively integrate with Ag/$ZnWO_4$ to form a nanocomposite which can lead to a useful structure for better photoluminescence sensing of Hg^{2+}. The verification of composition can also be supported by ICP measurement as shown in Table S1 (ESI†). The experiments were carried out to display the leaching of Ag metal during the synthesis of the nanocomposites. As can be seen from Table S1 (ESI†) the Ag/Zn ratios are very similar, which indicate that some of the Ag metal gets leached when g-C_3N_4 is attached to Ag/$ZnWO_4$. Due to this leaching of Ag metal, the surface area of both the nanocomposites did not increase appreciably which is reflected from the BET results.

Tungstate materials have been observed to display significant PL. Generally, the transmission efficiency and the recombination rate of the photoexcited electron–hole pairs play important roles in the improvement of the performance of the nanocatalysts. It is well known that the decreased rate of recombination *i.e.*, the enhanced separation of charges can be substantiated with the quenching in the PL intensities of the composite photocatalysts.[62] The PL intensity can be correlated with the radiative recombination of the charges as the recombination of the photo-excited electrons with holes relates to the PL emission intensity. Fig. 5A portrays the PL emissions of the as-prepared nanocomposites where a broad blue emission band in the range of 350–500 nm has been observed for $ZnWO_4$ nanorods and for the composite materials, located at around 408 nm when excited at 310 nm. A small emission band in the UV region centered at 345 nm, which originated from excitonic recombination corresponds to the near band-gap emission of $ZnWO_4$ whereas, the visible emission band corresponds to defects (oxygen vacancies).[63] Liu *et al.*[64] and Longo *et al.*[65] have shown that this broad emission generally originates from a typical multiphonon process where relaxation of excited electrons proceeds through multiple paths involving several energy states within

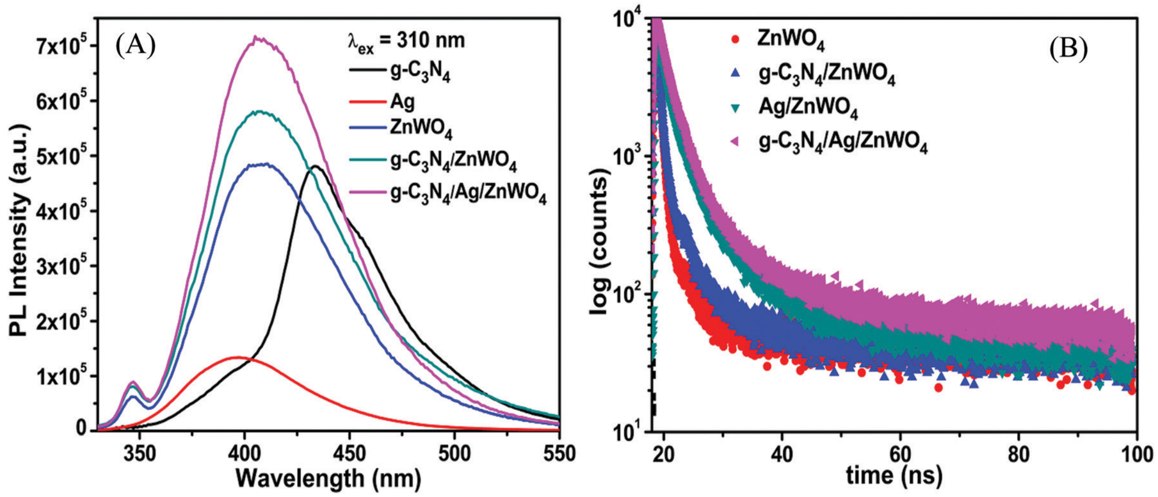

Fig. 5 (A) Room temperature PL emission spectra (λ_{ex} = 310 nm) of $ZnWO_4$ nanorods, g-C_3N_4/$ZnWO_4$ and g-C_3N_4/Ag/$ZnWO_4$ photocatalysts. (B) Time-resolved fluorescence decay spectra of pure $ZnWO_4$ and the various composited $ZnWO_4$ nanoparticles monitored at 310 nm by single-photon counting and excited by incident light of 330 nm from a picosecond-pulsed light-emitting diode at room temperature.

the bandgap. Thus, we can conclude from the position of the emission bands that the emissions from the composite materials are dominated by $ZnWO_4$ emission. This intrinsic blue emission band of $ZnWO_4$ originates from the charge transfer transition of the WO_6 octahedron.

The valence band (VB) and conduction band (CB) of $ZnWO_4$ are mainly constituted of the anti-bonding p-orbitals of O atoms and the 4d orbitals of W.[64] An unusual PL characteristic is displayed by $ZnWO_4$ where it is observed that its PL intensity is weaker than its corresponding composites g-C_3N_4/$ZnWO_4$ and g-C_3N_4/Ag/$ZnWO_4$, as shown in Fig. 5A. The enhanced emission by the nanocomposites can, therefore, be explained by the faster recombination of excited electrons and holes at the oxygen vacancy sites.[64] The spectra consist of two peaks, one peak in the UV region is located at 345 nm and the other is a broad emission band in the visible region centered at 408 nm. The UV emission band might have originated from excitonic recombination, which conforms to the near band edge emission of $ZnWO_4$.[63] The broad emission bands of the pure $ZnWO_4$ and its composites at 408 nm were Gaussian fitted (Fig. 6). Three-component peaks were located at ~390 nm, ~420 nm, and ~450 nm, respectively as presented in Fig. 6(A)–(C). The former two components belong to intrinsic photoluminescence of the WO_6 octahedron through non-radiative transition from $^3T_{1u}$ and $^1T_{1u}$ excited states to the ground state $^1A_{1g}$[64,66] while the peak at ~450 nm originated from the oxygen vacancy defects.[64] The third deconvoluted peak at ~450 nm is found to be blue-shifted for g-C_3N_4/Ag/$ZnWO_4$. deQuilettes *et al.*[67] have shown that the concomitant blue shift in the optical feature can modulate the intrinsic electronic structure near the band edge. The amount of oxygen vacancies in pure $ZnWO_4$ with respect to its composites at ~450 nm can be demonstrated by the ratio of the area of the component to that of the total area of the PL. Interestingly, it has been observed that the amount of oxygen vacancies gradually increased from 15.4% for $ZnWO_4$ to 19.3% for g-C_3N_4/$ZnWO_4$ to 24.6% for g-C_3N_4/Ag/$ZnWO_4$. The enhancement of oxygen vacancies in the $ZnWO_4$ of the composites was previously reflected in the HRTEM images in Fig. 3E and F and also obtained from XPS analysis (Fig. 4H). There is an intimate interaction among the (011) plane of $ZnWO_4$, the (022) of g-C_3N_4, and the (111) of Ag NPs. These intimate interactions improved the amount of oxygen vacancies as well as led to a deformed WO_6 octahedron, as reflected from the change of the shape of the composites.[64] Again, for the final composite material, the presence of oxygen vacancies has also been established through XPS analysis, as discussed earlier. The enhancement of the PL intensity can also

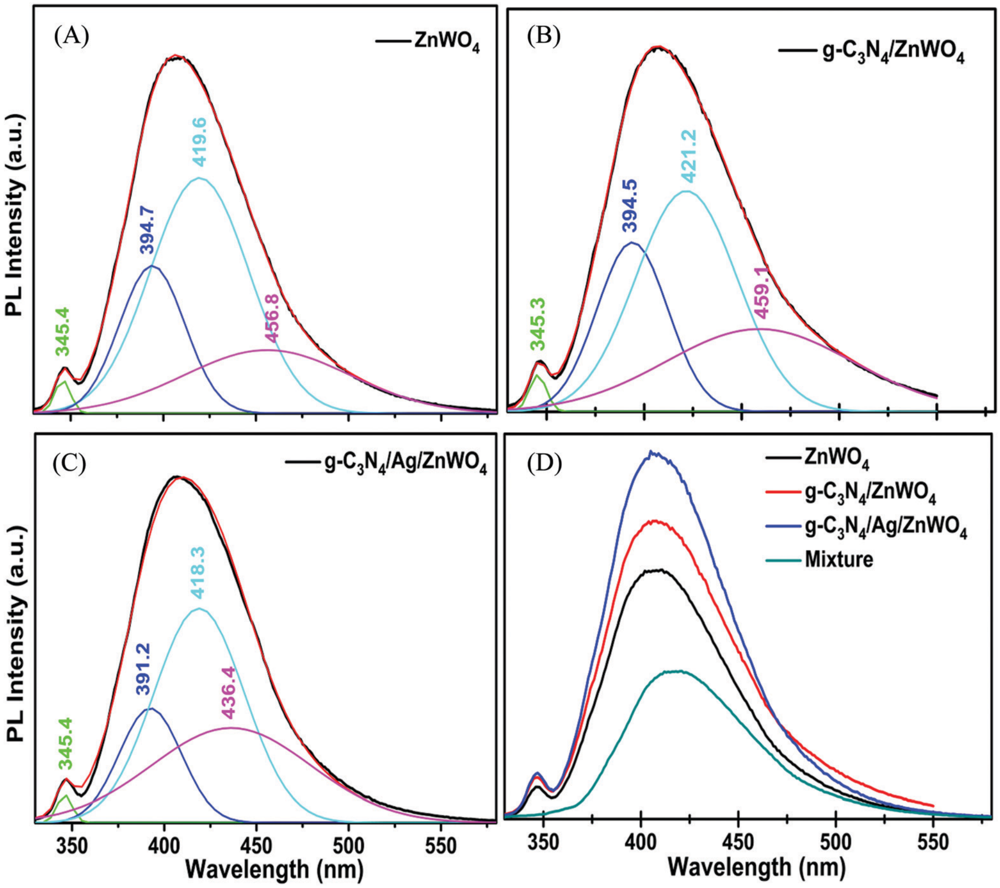

Fig. 6 PL spectra of (A) $ZnWO_4$, (B) g-C_3N_4/$ZnWO_4$, and (C) g-C_3N_4/Ag/$ZnWO_4$ deconvoluted with Gaussian fitting and (D) PL spectrum of a g-C_3N_4 + Ag + $ZnWO_4$ nanopowder mixture compared with the spectra of pure $ZnWO_4$ and the nanocomposites. The peak positions are obtained by fitting for clarity.

be ascribed to the localized surface plasmon resonance (LSPR) effect of Ag, which increases light absorption and thereby enhances exciton generation rate.[68] Furthermore, on compositing g-C_3N_4 with Ag/$ZnWO_4$, it is believed that strong coupling between the plasmonic field of Ag and the excitonic state of g-C_3N_4 is developed. This coupling is due to the propagation of oscillation of the plasmonic field and the excitons.[69,70] The oxygen defects on the surface of $ZnWO_4$ are, therefore, generated by the creation of oxygen vacancies by desorption of oxygen (after recombining with another oxygen atom). This increase of oxygen vacancies plays a crucial role in the enhancement of the PL intensities and thereby, can be used as a superior sensor towards Hg^{2+} sensing. For experimental evidence, we performed PL analysis of a sample containing $ZnWO_4$, g-C_3N_4, and Ag nanopowders, which were mechanically mixed and calcined at 220 °C for 4 h. We observed that the PL intensity of the mixture was lower than that of pure $ZnWO_4$ and the composites, as depicted in Fig. 6(D). This implies that the mechanical mixing simply generates a combination of distinctly separate phases and does not modify the surface of the phases.

To understand the increase of oxygen vacancies on the $ZnWO_4$ surface in pure $ZnWO_4$ and composites, we investigated the PL decay profiles as shown in Fig. 5B. The detailed PL decay profiles were obtained when the samples were monitored while exciting with a 330 nm monochromatic incident light from a light-emitting diode. An integrating sphere was used to prevent light scattering. The time-resolved fluorescence emission decays were fitted with the tri-exponential model and have been presented in Table S3 (ESI†) with their respective component percentages. The average lifetimes of the fluorescence decay for pure $ZnWO_4$ and the composites were found to be 6.5 ns and 10.7 ns, respectively. The average decay lifetimes were calculated from the following equation:

$$\langle\tau\rangle = \sum\alpha_i\tau_i^2/\sum\alpha_i\tau_i \quad (1)$$

where τ_i is the decay lifetime of the i-th component of the nanomaterials and α_i is the respective amplitude of the i-th component. The decay lifetime can be reflected as a combination of a fast decay component due to trap-assisted emission,[71,72] which corresponds to the recombination at the grain boundaries with the trap-states (oxygen vacancy sites) and a slow decay component that ascends due to the recombination of electron/hole pairs at the intrinsic electronic structure inside the grains *i.e.*, the radiative recombination. The fast and slow decays give a short lifetime (τ_1) and a long lifetime (τ_2), respectively. According to Yang *et al.*[73] and Zhang *et al.*[74] for an identical model, the trap-assisted recombination could describe the primarily non-radiative recombination between the charge carriers and the PL decay lifetime in the metal tungstates. From the PL decay profile, it is observed that g-C_3N_4/Ag/$ZnWO_4$ demonstrates an increase in α_2 and τ_2 values of 24.5% and 15.4 ns, respectively with respect to 15% and 9.6 ns, respectively for $ZnWO_4$. This increase of the slow decay component corresponds to the enhanced radiative recombination. Interestingly, a similar observation has been noticed for the fast decay component. Moreover, the enhancement of α_1 along with τ_1 for $ZnWO_4$ and g-C_3N_4/Ag/$ZnWO_4$ to that of α_2 and τ_2 is almost two-fold. This fact relies on better trap-assisted recombination, as reflected from the PL spectra concerning the radiative recombination between the intrinsic electronic states. It is noticed that there is no such contribution of the third component to the lifetime of the samples. Again, the enhanced QY from 6.6% to 11.4% (Fig. S4 and Table S2, ESI†) can also be attributed to the enhanced non-radiative recombination process associated with the surface-related traps.[64] Klimov and his co-worker[75] showed an interesting observation of large "global" Stokes shift between the emission band and the absorption band edge, that is indicative of the involvement of intra-gap trap in the PL process. Therefore, it can be concluded that for better catalytic performances by the nanocomposites there must be a balancing state between the trap-assisted (here, due to oxygen vacancies) recombination and the radiative recombination. This prolonged lifetime is therefore not only due to size-dependent emission but also involves enhanced oxygen vacancies on the surface of $ZnWO_4$ in the composites.

Fluorescence Hg^{2+} sensing

To govern the efficient detection of the toxic Hg^{2+} ion, the dispersion of the as-prepared nanoparticles has been tested in several solvents such as ethanol, methanol, ethylene glycol, water, DMF, and DMSO. It was found that the homogeneity (dispersion) of the NPs was best in the aqueous medium and hence, both PL and UV-Vis spectroscopy were performed in aqueous medium for the detection of Hg^{2+} ions.

Fig. 7A represents the gradual PL quenching of the g-C_3N_4/Ag/$ZnWO_4$ composite on successive addition of 2 μL each of Hg^{2+} solution (with concentration varying from 1 μM to 0.001 M of Hg^{2+}) to a 2 mL aqueous aliquot mixture containing 1 mg of g-C_3N_4/Ag/$ZnWO_4$ (excited at 310 nm). Therefore, the Hg^{2+} concentration can effectively be calculated by 2 μL × b μM/2000 μL = b nM (where b is the conc. of Hg^{2+} solution added). The emission peak was observed at 408 nm when excited at 310 nm. To get a better understanding of the complexation (static) quenching mechanism, the relative change in fluorescence intensities of g-C_3N_4/Ag/$ZnWO_4$ has been plotted as a function of quencher concentration, which reveals a linear relationship as described by the Stern–Volmer (SV) equation: $(I_{F_0}/I_F) = 1 + K_{SV}[Q]$ where, I_{F_0} and I_F are the fluorescence intensities in the absence and presence of quencher, respectively, K_{SV} is the Stern–Volmer constant and [Q] is the quencher concentration. This is also supported by the UV-Vis (Fig. S11B, ESI†) absorbance plots of g-C_3N_4/Ag/$ZnWO_4$, with the peak at 400 nm (broad peak) gradually disappearing and the peak at 306 nm getting wiped out after successive addition of Hg^{2+} solution at pH = 7.2, confirming the ground state adduct of Hg^{2+} with g-C_3N_4/Ag/$ZnWO_4$. The PL performance (Fig. 7C) of g-C_3N_4/Ag/$ZnWO_4$ for the detection of Hg^{2+} ion in local tap water was investigated however, no Hg^{2+} was detected. To validate the practical applicability of g-C_3N_4/Ag/$ZnWO_4$ as an Hg^{2+} sensor, this sample (local tap water) was spiked with Hg(II) salt. Before spiking, the sample was kept stagnant for a few hours. Encouraging results have been obtained showing similar behavior to those obtained under the standard conditions with distilled water. From the plot of

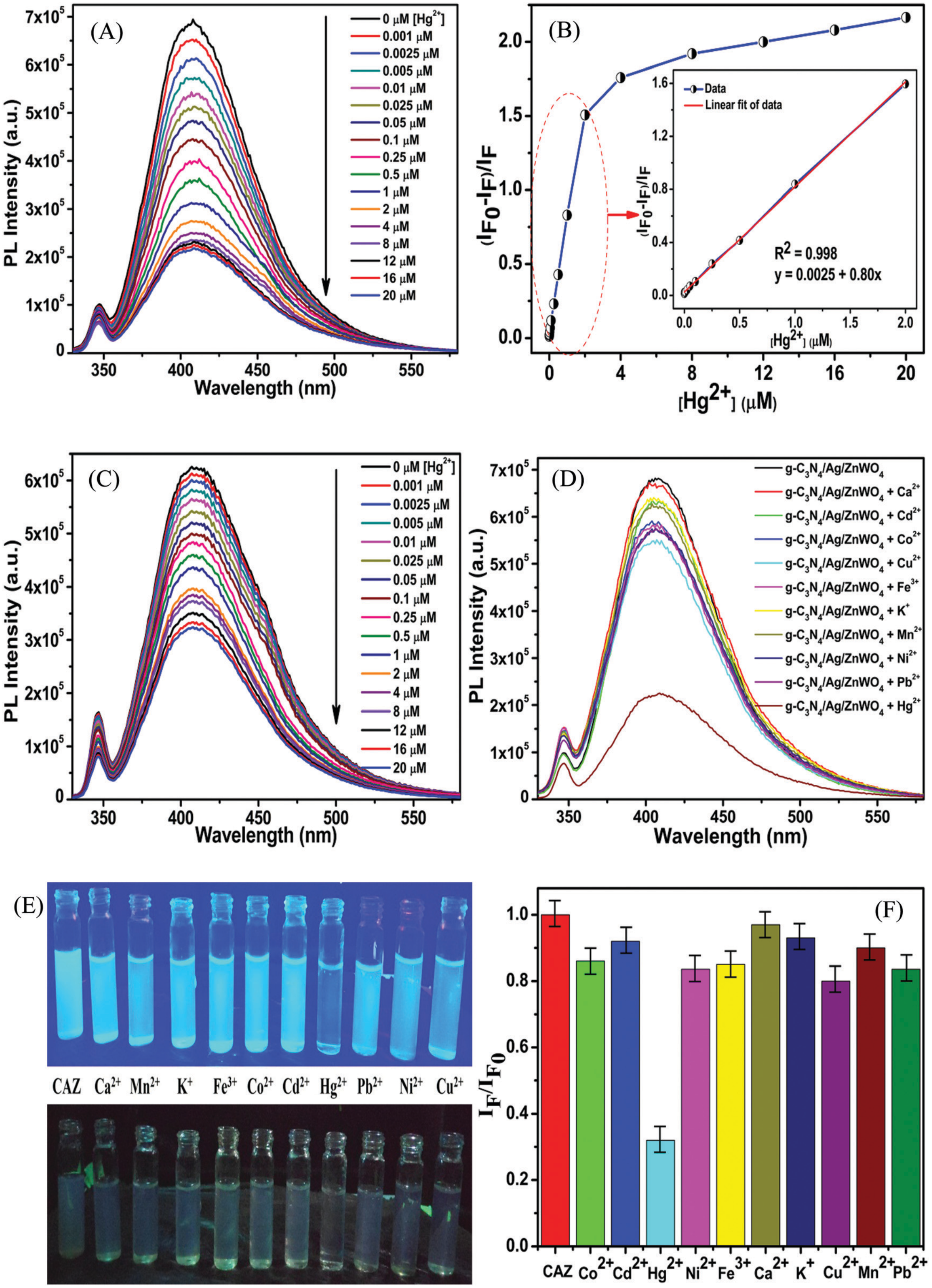

Fig. 7 (A) and (C) PL intensity responses of g-C_3N_4/Ag/$ZnWO_4$ in phosphate buffer (pH = 7.2) and tap water, respectively on the addition of different amounts of Hg^{2+}, λ_{ex} = 310 nm, (B) calibration curve of g-C_3N_4/Ag/$ZnWO_4$ for the detection of Hg^{2+} (inset is a linear plot of relative intensity *vs.* conc. of Hg^{2+}), (D) PL emission of g-C_3N_4/Ag/$ZnWO_4$ in the presence of different metal ions individually (λ_{ex} = 310 nm, [M^{n+}] = 10 μM), (E) photographic image of g-C_3N_4/Ag/$ZnWO_4$ in phosphate buffer under 365 nm light (upper panel) and white light in the presence of different metal ions (10 μM) (lower panel), and (F) bar diagram of the relative PL emission intensities (I_F/I_{F_0}) of g-C_3N_4/Ag/$ZnWO_4$ in the presence of various metal ions (10 μM).

the calibration curve (Fig. 7B), it was noticed that there is a linear growth in quenching at lower concentrations of the quencher (Hg^{2+}) while the quenching saturated quickly at higher concentrations of the quencher. The linear range for the quantitative Hg^{2+} sensing was found to be 0 nM–2 μM for both the cases of distilled water and tap water (Fig. S8B, ESI†). As per WHO standards, the limiting concentration to detect Hg^{2+} is 10 nM[14] but in this case, the detection limit (LOD) was estimated to be 0.23 nM (S/N = 3.0) in distilled water which is a very low value in comparison to the standard value. But for tap water, the LOD (Fig. S8B, ESI†) was found to be slightly higher with a value of 0.27 nM. Therefore, it can be concluded that our system is highly sensitive towards Hg^{2+} ions. The efficiency of the sensing capability of the samples increases with the composition of $ZnWO_4$ with g-C_3N_4 and Ag since the active surface area of the composites increases with that of $ZnWO_4$ as mentioned previously. This high efficiency of the final composite material may also be partially attributed to the increased oxygen vacancies on the $ZnWO_4$, which can serve as traps for photo-generated electron–holes, and are thus believed to play a very important role in PL sensing of Hg(II). With some selected literature reports, Table S5 (ESI†) represents the comparison of g-C_3N_4/Ag/$ZnWO_4$ with several other nanomaterials developed earlier for Hg^{2+} detection. It can be observed that the prepared nanocomposite has the potential to be a promising Hg^{2+} sensor. Similarly, the quantitative detection of Hg^{2+} by $ZnWO_4$ and g-C_3N_4/$ZnWO_4$ was performed and shown in Fig. S7(A) and (B) (ESI†), respectively and the calibration curves (Fig. S8A, ESI†) indicate the precision of detection limit and the linear range of sensing. A comparison chart for the detection of Hg^{2+} has been presented in Table 1 which reflected the development of the nanocomposite from $ZnWO_4$ to g-C_3N_4/Ag/$ZnWO_4$.

The high selectivity of g-C_3N_4/Ag/$ZnWO_4$ towards Hg^{2+} ions as compared with the other metal ions (M^{n+} = Ca^{2+}, Cd^{2+}, Fe^{2+}, Co^{2+}, Cu^{2+}, K^+, Mn^{2+}, Ni^{2+}, and Pb^{2+}) can be well justified from the PL plots (Fig. 7D and corresponding bar diagram Fig. 7F) and the photographic image (Fig. 7E), upon addition of 10 μM metal ion solution under identical conditions. It is clearly visible that the Hg^{2+} ions quenched the PL spectrum of g-C_3N_4/Ag/$ZnWO_4$ most effectively, while the other metal ions had no noticeable significance on PL. It was however, observed that the prior addition of other metal ions (M^{n+}) to g-C_3N_4/Ag/$ZnWO_4$ solution somewhat affects the PL quenching by Hg^{2+} (from Fig. S5, ESI†). Nevertheless, with the quenching of PL by Hg^{2+} being high, the presence of other metal ions does not hamper the detection of Hg^{2+}. The ability of nitrogen heteroatoms in g-C_3N_4 to behave as Lewis bases suggests that the presence of transition metals might lead to the coordination with nitrogen heterocyclics. Such coordination, however, may not occur with the other metal ions. The interaction of the soft Hg(II) with moderately hard nitrogen donor atoms of the heterocyclics is the basis for our approach in developing a detection method.[76] V. K. Harika *et al.* have shown that there is an obvious slight charge transfer between the electron donor (N atom of g-C_3N_4) to the acceptor (Hg^{2+}) by XANES analysis.[32] The reason for the selective detection of Hg(II) can also be explained based on the reduction potential of the metal ions tested. Reduction potential values of the various ions may help to understand why Hg^{2+} is preferentially grafted. Red. pot. values of the following cations (V *vs.* NHE) are as follows: $Ca^{2+}/Ca = -2.84$, $Cd^{2+}/Cd = -0.403$, $Fe^{2+}/Fe = -0.44$, $Co^{2+}/Co = -0.277$, $Cu^{2+}/Cu = 0.340$, $K^+/K = -2.924$, $Mn^{2+}/Mn = -1.17$, $Ni^{2+}/Ni = -0.257$, $Pb^{2+}/Pb = -0.126$, $Hg^{2+}/Hg = 0.8535$. It is seen that the red. pot. value of Hg^{2+} is the most positive among the mentioned metal ions hence, it will get reduced most quickly. Therefore, it will attach most efficiently to any electron donor species; in our case, it will easily coordinate with the lone pairs of the nitrogen of g-C_3N_4 in comparison to the other metal ions that have been tested.[38,39] The extent of PL quenching by Hg^{2+} ions decrease in the presence of other metal ions in the reaction medium due to their blocking or engagement of the binding sites present on the surface of the g-C_3N_4/Ag/$ZnWO_4$ fluorophore sensor.[33,77] However, this does not affect the detection of Hg^{2+} appreciably as observed from the bar diagram in Fig. 7F. Hence, the as-synthesized material can be used for the selective detection of Hg^{2+}. The Hg(II) ions coordinated with the N atom of the heterocyclic g-C_3N_4 are evident from the XPS (Fig. S6A, ESI†) which substantiates the selectivity of Hg(II) *versus* other metal ions tested. When XPS analysis of g-C_3N_4/Ag/$ZnWO_4$ was performed after adding Hg(II) salt in the presence of other metal ions, two peaks for Hg(II) were observed at the binding energies of 100.4 eV and 104.6 eV for Hg(II) $4f_{7/2}$ and $4f_{5/2}$, respectively (Fig. 8A). From the nature of the deconvoluted curves for N 1s in Fig. 8B, it is quite clear that the two spectra before and after the addition of Hg^{2+} are quite different, showing a shift in the binding energies. These observations infer that the binding of Hg^{2+} occurs with the N atoms of the heterocycle. Furthermore, the EDX result as shown in Fig. S6B (ESI†) also infers the presence of Hg(II) on the surface of the sensor.

The mechanistic pathway for the detection of Hg^{2+} can be attributed to Fig. 9A which indicates the effect of using the strong reducing agent $NaBH_4$ on PL quenched g-C_3N_4/Ag/$ZnWO_4$ by Hg^{2+}. The photographic depiction of PL quenching of g-C_3N_4/Ag/$ZnWO_4$ by 10 μM Hg^{2+} has been presented in Fig. 9B. However, on introducing the strong reducing agent $NaBH_4$ in the above quenched solution the fluorescence intensity increased sharply. This might be due to the reduction of Hg^{2+} to Hg(0) by $NaBH_4$ which resulted in the loss of complexation between Hg^{2+} ions and the composite. This regaining back to the pure composite leads to retrieval of the PL intensity. We have examined the formal oxidation state of Hg(II) in the sensing medium after the addition of BH_4^- so that we can scrutinize the effect of reducing agent on Hg(II). The XPS of Hg(II) 4f could be deconvoluted to two doublets with binding energies of 99.9 eV and 104.3 eV. The fitted curves at the higher binding energy correspond to Hg^{2+} while the lines at lower energy are attributed

Table 1 Linear range and detection limit comparisons for Hg^{2+} sensing by the nanoparticles

Samples	Linear range	R^2	Detection limit
$ZnWO_4$	25 nM–0.1 μM	0.9905	25.0 nM
g-C_3N_4/$ZnWO_4$	1 nM–1 μM	0.9888	4.8 nM
g-C_3N_4/Ag/$ZnWO_4$	0 nM–2 μM	0.9980	0.23 nM

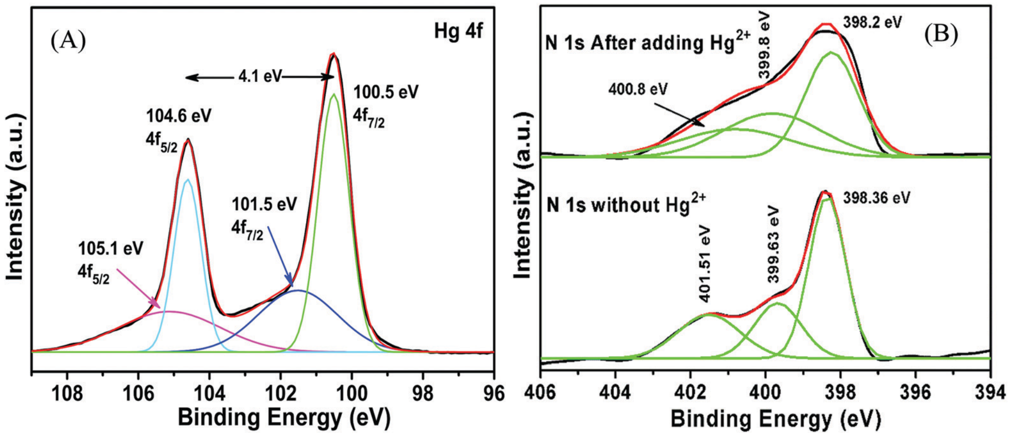

Fig. 8 XPS analysis of g-C_3N_4/Ag/$ZnWO_4$ after adding Hg(II) salt in the presence of other metal ions (A) Hg 4f; (B) N 1s.

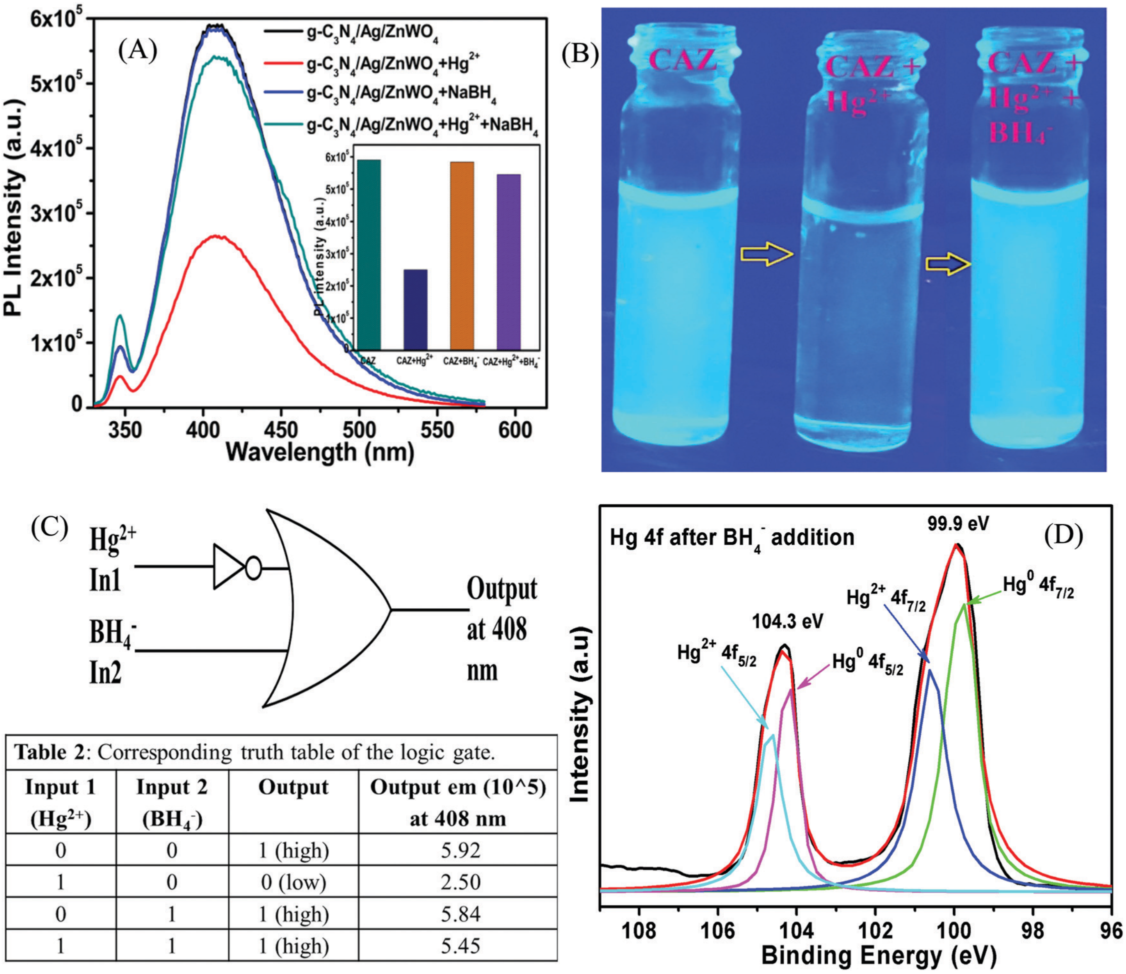

Table 2: Corresponding truth table of the logic gate.

Input 1 (Hg^{2+})	Input 2 (BH_4^-)	Output	Output em (10^5) at 408 nm
0	0	1 (high)	5.92
1	0	0 (low)	2.50
0	1	1 (high)	5.84
1	1	1 (high)	5.45

Fig. 9 (A) PL effect of $NaBH_4$ on g-C_3N_4/Ag/$ZnWO_4$-Hg^{2+}. (B) Photographic image of experiment (A) under 365 nm light. (C) Implication logic gate obtained from the results of (A) and (D) X-ray photoelectron spectroscopy of Hg 4f after the addition of BH_4^-.

to Hg^0 as shown in Fig. 9D.[78,79] The characteristic peaks for Hg(0) and Hg(II) were generally witnessed at 99.7 eV/104.1 eV and 100.7 eV/104.5 eV respectively. This observation indicates the formation of AgHg amalgam after the addition of Hg(II) to the nanocomposites. Therefore, the presence of metallic Hg^0 confirms the reduction of Hg(II) by the reducing agent BH_4^- at the surface of the nanocomposites. Again, the spectra also predict that a very small amount of Hg(II) ions remain present in the

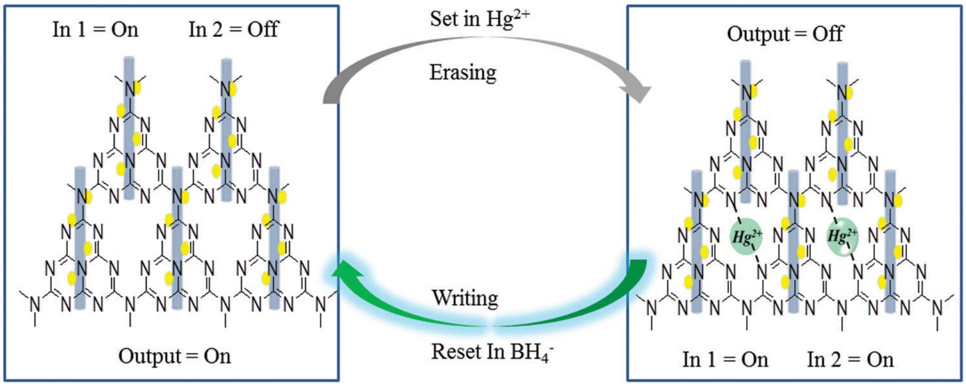

Scheme 2 Probable mechanistic pathway for the grafting of Hg^{2+} with g-C_3N_4/Ag/$ZnWO_4$ and further reduction of Hg^{2+} by $NaBH_4$, correlated with Implication Logic Gate.

sensing medium that were not totally reduced by BH_4^-. This fact could be the reason that the PL intensity of the nanocomposite was not fully retrieved.

In other words, the grafting of the metal ions into the cavity of g-C_3N_4 (as shown in Scheme 2) do not take place in their elemental form, as the lone pairs of the N atoms in g-C_3N_4 are not able to coordinate with Hg(0), resulting in regaining the PL intensity. Hence, the g-C_3N_4/Ag/$ZnWO_4$ nanocomposite can act as a scavenger for Hg^{2+} ions. To study the binding site(s) and binding constant of g-C_3N_4/Ag/$ZnWO_4$ and Hg^{2+} a linear calibration curve obtained from the plot of $\log[(F_0 - F)/F]$ *vs.* $\log[Hg^{2+}]$ (Fig. S14, ESI†) is used to determine the slope (n), which indicated the binding site and the intercept gave the binding constant ($\log k$). The plot is obtained using the following eqn (2):[80]

$$\log[(F_0 - F)/F] = \log k + n\log[Hg^{2+}] \quad (2)$$

where, F_0 and F are the PL intensities of g-C_3N_4/Ag/$ZnWO_4$ without the quencher Hg^{2+} and with an intermediate concentration of the quencher, respectively. The complexation or binding constant and the binding site are found to be 10.6 and 1.7, respectively which signified the presence of only one type of binding site.[81]

The average PL emission decay lifetime increased from 8.00 ns to 8.59 ns for the g-C_3N_4/Ag/$ZnWO_4$ nanocomposite with the addition of a 10 μM Hg^{2+} solution, when excited with a 330 nm laser and the emission was monitored at 408 nm (Fig. S9, ESI†). The decay lifetime values are presented in Table S4 (ESI†). The decay lifetime of the g-C_3N_4/Ag/$ZnWO_4$ nanocomposite is increased by approximately 0.6 ns upon the addition of Hg^{2+}. This increase in lifetime might be due to the heavy metal atom effect. The presence of heavy metal atoms might lead to better intersystem crossing (ISC) from the excited singlet state to the triplet state (please refer to Fig. S9 and the discussion therein, ESI†).

Fig. S12 (ESI†) shows the PL emission spectra for different excitation wavelengths. The maximum emission occurred at $\lambda_{em} = 408$ nm when excited at $\lambda_{ex} = 310$ nm. The emission peaks for different excitation energies appeared at the same wavelength however, their intensities varied, which implied the samples are highly pure and did not decompose during light irradiation. Hg^{2+} sensing is especially dependent on the pH of the electrolyte solution. The PL emission intensities of the Hg^{2+} sensor at different pH have been illustrated in Fig. S10A (ESI†) and the bar diagram (Fig. S10B, ESI†) represented the extent of PL quenching. The pH optimization was studied in the pH range of 3.0 to 10.0. The results depicted that the fluorescence emission peak intensities did not change much in the pH range from 3.0 to 6.0, after which the intensities decreased reasonably. The maximum PL quenching is observed for pH 7.2, *i.e.*, at neutral pH. The quenching decreased again at higher pH. So, the optimized pH was taken to be 7.2 and the ensuing experiments were carried out at this pH. Again consistant with the fluorescence spectra, the absorbance spectra of g-C_3N_4/Ag/$ZnWO_4$, at pH 3.0, 7.2, and 10.0 in the absence and presence of Hg^{2+} ion, (Fig. S11A, ESI†), clearly showed that the peak at 306 nm completely disappeared on the addition of Hg^{2+} at pH 7.2, while no change was observed for the two peaks at pH of 3.0 and 10.0, respectively. The maximum quenching indicates that the major ground state adduct formation between Hg^{2+} and the NPs took place at pH 7.2. The adduct formation was quite low at other pH values. In the acidic pH range, positive charges were generated on the surface of the NPs which reduced the surface association of g-C_3N_4/Ag/$ZnWO_4$ with a similarly charged heavy metal ion (Hg^{2+}), leading to less sensitivity. While under basic conditions Hg^{2+} tends to combine with OH^- to form $Hg(OH)_2$ or H-bonding agglomerates, resulting in a decreased sensitivity.[37] To confirm the fluorescence stability of g-C_3N_4/Ag/$ZnWO_4$ time-dependent fluorescence quenching by Hg^{2+} was studied for 10 min and the results are shown in Fig. S13 (ESI†). Immediately after the addition of Hg^{2+} at room temperature, the fluorescence intensity of the NPs dropped sharply and then became constant thereafter. It can thus be inferred that the NPs were highly fluorescently stabilized.

The PL sensing of Hg(II) by the nanocomposites g-C_3N_4/Ag/$ZnWO_4$ was repeated several times. Fig. S16 (ESI†) defines the efficiency of resetting the system over multiple cycles. We can see that the PL intensity decreases sharply after adding 2 μM of Hg(II) solution and immediately regained the initial PL intensity with the addition of a very little amount of $NaBH_4$ solution (0.5 μM). Therefore, from the above observation, we can conclude that the device is capable of being reset. A slight decrease of ∼1.1% in efficiency was observed after the 12th cycle. By doing so, the composition (Fig. S17C, ESI†) and the morphology (Fig. S17A and B, ESI†) of the nanocomposites remained unchanged after multiple cycles of Hg(II) sensing. The morphology of the nanocomposites was found to be 'square plate' like.

Probable mechanistic study of fluorescence

The PL excitation spectrum (Fig. S15A, ESI†) for g-C_3N_4/Ag/$ZnWO_4$ (black line) showed two peaks at 306 and 370 nm, respectively. The higher contribution to the PL emission spectrum (red line) at 408 nm, as already mentioned, was from the 306 nm excitation. The blue line in Fig. S15A (ESI†) represented room temperature phosphorescence (RTP) when excited at 310 nm, which can also be observed in the excitation dependent (Fig. S15B, ESI†) RTP of the composite material. However, the phosphorescence intensity was very low. For organic molecules, the RTP is mainly due to surface C═O/C═N.[82–84] The obtained low intense phosphorescence might be due to the presence of a heavy atom (Ag) in the composite material. This low intense RTP could be attributed to the outcome of a few factors, (i) ineffective intersystem crossing (ISC) between the excited singlet states to the triplet state, (ii) non-radiative decay,[78] and (iii) quenching of the triplet state. The phosphorescence could be increased by enhancing the intersystem crossing when the states involved in the emission process could undergo spin–orbit coupling. In the present work, as the material contains Ag, we believe the spin–orbit coupling is affected by the wide separation in energy between the singlet and triplet states. Also, the presence of oxygen in $ZnWO_4$ in the composite cannot prevent quenching of the triplet state, resulting in low intense RTP. The phosphorescence mechanism process could be explained by the energy level diagram as shown in Scheme S1 (ESI†). The electronically excited states S_1 and T_1 were obtained by n–π* transition and likewise π–π* transition for S_2 and T_2 of g-C_3N_4. Therefore, the transition from the ground state (S_0) to the excited singlet state *i.e.* S_0–S_1 and S_0–S_2 in Scheme S1 (ESI†) could be correlated to 306 nm and 383 nm wavelengths, respectively in the excitation absorption spectrum in Fig. 1B. These peaks were well justified with 310 nm and 366 nm wavelengths, respectively in the PL excitation spectrum shown in Fig. S15A (ESI†) (black curve). So, it indicated that the excitation at 310 nm suggested S_0–S_2 *i.e.* π–π* transition that could be dominant in contributing to the fluorescence and phosphorescence processes. But the RTP intensity was quite low in comparison to the fluorescence. The PL intensity and the lifetime increases with successive addition of g-C_3N_4 and Ag NPs to $ZnWO_4$, which help to attain optimum oxygen vacancies on the $ZnWO_4$ surface. The PL emission S_n–S_0 peak was obtained at 408 nm while the phosphorescence commenced from ∼520 nm. This wide energy gap between the excited singlet states to excited triplet states might lead to constrained ISC, which is likely to cause less population at the excited triplet state. Therefore, the low intense RTP (T_1–S_0) might be solely due to the electrons present in the excited triplet state in which some vibrational relaxation and internal conversion (IC) take place. RTP could also be prevented due to non-radiative decay, such as vibrational relaxation (VR) and static quenching effects.[37] Therefore, in the presence of Hg^{2+}, there was no phosphorescence peak due to the heavy metal effect.

Detection of Hg^{2+} ion in real samples

To validate the practicability of the proposed sensing method, the detection of Hg^{2+} ions in real samples collected from different sources like pond water, sewage water around Kolkata, and waste CFL bulbs was determined. The water samples were filtered using a 0.22 micrometer membrane several times to remove all the suspended particulate and dirt particles. The pond water was spiked with Hg^{2+} salt so that a known concentration of Hg(II) solution is obtained and can be estimated with our proposed method. Generally, the CFL bulbs contain 4 mg of Hg. This mercury was extracted by a chemical method of the efficacy of broken glass, as shown in Fig. S18 (ESI†). All measurements were performed at least thrice and the analytical results are displayed in Table 2. The results of the real samples were obtained with RSD values ranging from 0.64 to 1.12. The above results confirm that our proposed method effectively analyzes trace levels of Hg^{2+} in real samples.

Method comparison

Table 3 displays a comparison between several other methods with the present method, by which Hg^{2+} ions were detected. As can be seen from the list, the present method has provided either similar or superior reproducibility and/or sensitivity than that reported by others. The conventional methods like ICPMS and AAS/AES *etc.* are of limited availability and require sophisticated and costly instrumentation and intricate sample preparation.[85,86] However, the LOD and % RSD obtained in our case were lower than the other listed methods. Based on these results, the fluorescence method would, therefore, be a reasonable approach to monitor Hg^{2+} sensing.

Designing a molecular memory device

A memory device could be constructed using a molecular information processing technique for Hg^{2+} ion interaction with g-C_3N_4/Ag/$ZnWO_4$. The optical outputs of the receptor g-C_3N_4/Ag/$ZnWO_4$ could be utilized to develop a logic device by taking Hg^{2+} as input 1 and BH_4^- as input 2 at the molecular level and monitor the changes of fluorescence as the output. An Implication logic (Fig. 9C) behavior based on PL response profile (from Fig. 9A and the inset bar diagram) towards Hg^{2+} detection is observed at the emission wavelength of 408 nm. A truth table for this logic gate can be constructed and is presented in Table 2

Table 2 Analysis of Hg^{2+} in real samples

Sample	Hg^{2+} spiked (nM)	Hg^{2+} estimated by PL method	Recovery%	RSD%	ICP-MS analysis
Pond water	10	9.93 nM	99.3	0.82	—
	20	19.74 nM	98.7	0.64	—
	40	39.3 nM	98.3	1.12	—
Sewage water	—	3.7 mg L^{-1}	97.4	0.91	3.8 mg L^{-1}
CFL bulbs (3 pcs)	—	8.52 mg L^{-1}	98.8	0.77	8.62 mg L^{-1}

Table 3 Comparison of different reported methods of analysis for Hg^{2+} ions

Sample	Method	Linear range	LOD (nM)	RSD%	Ref.
F-MWCNT/Fe_3O_4/0.5% Nafion/GCE	GCE[a]	0.013–32.5 μg L^{-1}	3.9	1.19	87
Fe_3O_4@SiO_2@γ-MPTS MNPs	MSPE-ICP-MS[b]	5–5000 ng L^{-1}	3.7	2.7	88
MGO-DVB-VA	MSPE-FAAS[c]	—	1.85	3.1	88
MNPs–PAMAM-Gn	MSPE-HPLC-VWD[d]	0.1–200 μg L^{-1}	0.40	1.93	88
Ag NPs	Colorimetric	0.5 nM–500 μM	31	<2	89
Gold nanostars (AuNSs)/CE	SWASV[e]	0.75 nM–26 μM	2.5	3.2	90
Dextran functionalized Ag/Cu NCs	Optical Spectroscopy	20–100 nM	10	—	91
Cysteamine (CA)-capped CdTe QDs	Fluorescence	6 nM–450 nM	4	—	92
g-C_3N_4/Ag/$ZnWO_4$	Fluorescence	0–2 μM	0.23	<1	This work

[a] Modified glassy carbon electrode. [b] Magnetic solid-phase extraction. [c] Flame atomic absorption spectrometry. [d] Variable wavelength detector. [e] Square-wave anodic stripping voltammetry.

of Fig. 9C. The output "0" represented the "low state" for the quenching of PL intensity after the addition of Hg^{2+} while, the output "1" represented the "high state" in the presence or absence of both the inputs. The receptor gets free immediately after the addition of the strong reducing agent $NaBH_4$ to the solution containing the Hg^{2+} ion. Accordingly, a probable mechanistic pathway for the grafting of Hg^{2+} with the receptor and the 'set–reset' or 'erasing–writing' process using the logic device has also been depicted in Scheme 2.

Conclusion

In summary, a unique nanocomposite consisting of a stoichiometric amount of Ag with $ZnWO_4$ nano-rods composited with g-C_3N_4 has been developed using a simple hydrothermal technique that has made it a sustainable and environmentally friendly method. The as-synthesized materials were vividly characterized to confirm the formation and unique physiochemical properties of the nanocomposites. A selective test for the heavy metal ion sensing has been performed in solution by PL spectroscopy, where the fluorophore g-C_3N_4/Ag/$ZnWO_4$ was found to be highly sensitive towards Hg^{2+} through metallophillic interaction and displayed a static quenching mechanism at the emission wavelength of 408 nm. The maximum PL sensitivity for Hg^{2+} at a pH of 7.2, suggests that it could be a potential tool for Hg^{2+} ion detection in a biological fluid upon further modification. The high sensitivity of the hybrid material was found to be 0.23 nM in the wide linear range of 0 nM to 2 μM. Furthermore, a few real samples were applied to detect Hg^{2+} by this proposed method that has significant solicitation in routine Hg^{2+} analysis. The proposed grafting mechanism could well be justified when $NaBH_4$ was added in the dispersed solution of g-C_3N_4/Ag/$ZnWO_4$ in the presence of Hg^{2+} ion by which a response profile at the emission wavelength and a logic device of Implication gate could also be developed.

Furthermore, the hybrid material was found to be RTP active but its intensity was low. To get a better RTP, the triplet state of the organic part of the composite material needs to be stabilized, which requires further exploration of g-C_3N_4.

Conflicts of interest

The authors declare no competing financial interest.

Acknowledgements

The authors acknowledge the financial support from MHRD-India for instrumental facilities to the Department of Chemistry, IIEST, Shibpur. The authors, U. K. Ghorui and P. Mondal are thankful for the financial assistantship and instrumental facilities from IIEST, Shibpur. J. Satra and Dr S. Mardanya are grateful to UGC-RGNF (fellowship id: 201516-RGNF-2015-17-SC-WES-690), India, and SERB-NPDF (PDF/2016/002319), India, respectively for their financial assistance.

References

1 P. A. Ariya, M. Amyot, A. Dastoor, D. Deeds, A. Feinberg, G. Kos, A. Poulain, A. Ryjkov, K. Semeniuk, M. Subir and K. Toyota, *Chem. Rev.*, 2015, **115**, 3760–3802.
2 G. Chen, Z. Guo, G. Zeng and L. Tang, *Analyst*, 2015, **140**, 5400–5443.
3 J. H. Duffus, *Pure Appl. Chem.*, 2002, **74**, 793–807.
4 G. Aragay, J. Pons and A. Merkoci, *Chem. Rev.*, 2011, **111**, 3433–3458.
5 J. Li, J. Yao and W. Zhong, *Chem. Commun.*, 2009, 4962–4964.
6 H. J. Chun, S. Kim, Y. D. Han, D. W. Kim, K. R. Kim, H.-S. Kim, J.-H. Kim and H. C. Yoon, *Biosens. Bioelectron.*, 2018, **104**, 138–144.
7 Y. Gao, Z. M. Shi, Z. Long, P. Wu, C. B. Zheng and X. D. Hou, *Microchem. J.*, 2012, **103**, 1–14.
8 I. Lehnherr, V. L. S. Louis, H. Hintelmann and J. L. Kirk, *Nat. Geosci.*, 2011, **4**, 298–302.
9 Y. Horowitz, D. Greenberg, G. Ling and M. Lifshitz, *Arch. Dis. Child.*, 2002, **86**, 453–455.
10 R. A. Bernhoft, *J. Environ. Public Health*, 2012, 460508, DOI: 10.1155/2012/460508.
11 S. Bose-O'Reilly, K. M. McCarty, N. Steckling and B. Lettmeier, *Current Problems in Pediatric and Adolescent Health Care*, 2010, **40**, 186–215.
12 M. Harada, *Crit. Rev. Toxicol.*, 1995, **25**, 1–24.
13 S. W. Tan, J. C. Meiller and K. R. Mahaffey, *Crit. Rev. Toxicol.*, 2009, **39**, 228–269.
14 *Guidelines for Drinking Water Quality*, World Health Organization, Geneva, 3rd edn, 2004, p. 188.
15 E. M. Nolan and S. J. Lippard, *Chem. Rev.*, 2008, **108**, 3443–3480.

16 L. R. Adil, P. Gopikrishna and P. K. Iyer, *ACS Appl. Mater. Interfaces*, 2018, **10**, 27260–27268.

17 S. Bhatt, M. Bhatt, A. Kumar, G. Vyas, T. Gajaria and P. Paul, *Colloids Surf., B*, 2018, **167**, 126–133.

18 A. Kumar, M. Bhatt, G. Vyas, S. Bhatt and P. Paul, *ACS Appl. Mater. Interfaces*, 2017, **9**, 17359–17368.

19 T. Guo, J. Baasner, M. Gradl and A. Kistner, *Anal. Chim. Acta*, 1996, **320**, 171–176.

20 H. Wang, B. Kang, T. F. Chancellor, T. P. Lele, Y. Tseng and F. Ren, *Appl. Phys. Lett.*, 2007, **91**, 042114–042116.

21 H. Li, J. Zhai, J. Tian, Y. Luo and X. Sun, *Biosens. Bioelectron.*, 2011, **26**, 4656–4660.

22 G. Vyas, S. Bhatt and P. Paul, *ACS Omega*, 2019, **4**, 3860–3870.

23 S. H. Yu, B. Liu, M. S. Mo, J. H. Huang, X. M. Liu and Y. T. Qian, *Adv. Funct. Mater.*, 2003, **13**, 639–647.

24 J. H. Pan, H. Dou, Z. Xiong, C. Xu, J. Ma and X. S. Zhao, *J. Mater. Chem.*, 2010, **20**, 4512–4528.

25 H. Kadowaki, N. Saito, H. Nishiyama, H. Kobayashi, Y. Shimodaira and Y. Inoue, *J. Phys. Chem. C*, 2007, **111**, 439–444.

26 R. Lacomba-Perales, J. Ruiz-Fuertes, D. Errandonea, D. Martínez-García and A. Segura, *Europhys. Lett.*, 2008, **83**, 37002–37018.

27 M. I. Osotsi, D. K. Macharia, B. Zhu, Z. Wang, X. Shen, Z. Liu, L. Zhang and Z. Chen, *Mater. Res. Bull.*, 2007, **42**, 696–706.

28 T. Montinia, V. Gombaca, A. Hameeda, L. Felisarid, G. Adamia and P. Fornasiero, *Chem. Phys. Lett.*, 2010, **498**, 113–119.

29 C. Liu, C. Huang and H. Chang, *Langmuir*, 2008, **24**, 8346–8350.

30 Y. Zheng, C. Chen, Y. Zhan, X. Lin, Q. Zheng, K. Wei and J. Zhu, *J. Phys. Chem. C*, 2008, **112**, 10773–10777.

31 Y. Zhang, N. Feng, S. Zhou and X. Xin, *Nanoscale*, 2021, **13**, 4140–4150.

32 V. K. Harika, T. R. Penki, B. Loukya, A. Samanta, G.-L. Xu, C.-J. Sun, I. Grinberg, F. L. Deepak, K. Amine, D. Aurbach and A. Gedanken, *Chem. Sci.*, 2021, **12**, 3226–3238.

33 Y. Li, J.-F. Xie, C.-C. Chang, C.-M. Wang and H.-L. Tu, *ACS Appl. Nano Mater.*, 2020, **3**, 9724–9730.

34 A. J. Wang, H. Li, H. Huang, Z. S. Qian and J. J. Feng, *J. Mater. Chem. C*, 2016, **4**, 8146–8160.

35 Y. Dong, Q. Wang, H. Wu, Y. Chen, C. H. Lu, Y. Chi and H. H. Yang, *Small*, 2016, **12**, 5376–5393.

36 B. Luo, S. Liu and L. Zhi, *Small*, 2012, **8**, 630–646.

37 K. Patir and S. K. Gogoi, *ACS Sustainable Chem. Eng.*, 2018, **6**, 1732–1743.

38 S. Ebrahim, A. Shokry, M. M. A. Khalil, H. Ibrahim and M. Soliman, *Sci. Rep.*, 2020, **10**, 13617.

39 C. V. Raju and S. S. Kumar, *Sci. Rep.*, 2021, **11**, 6932.

40 P. A. de. Silva, N. H. Q. Gunaratne and C. P. McCoy, *Nature*, 1993, **364**, 42–44.

41 B. Daly, J. Ling and P. A. de. Silva, *Chem. Soc. Rev.*, 2015, **44**, 4203–4211.

42 B. Ghaemi, E. Shaabani, R. Najafi-Taher, S. J. Nodooshan, A. Sadeghpour, S. Kharrazi and A. Amani, *ACS Appl. Mater. Interfaces*, 2018, **10**, 24370–24381.

43 F. Wang, W. Li, S. Gu, H. Li, X. Liu and M. Wang, *ACS Sustainable Chem. Eng.*, 2016, **4**, 6288–6298.

44 J. Lin, J. Lin and Y. Zhu, *Inorg. Chem.*, 2007, **46**, 8372–8378.

45 L. Ma, H. Fan, K. Fu, S. Lei, Q. Hu, H. Huang and G. He, *ACS Sustainable Chem. Eng.*, 2017, **5**, 7093–7103.

46 J. Xue, S. Ma, Y. Zhou, Z. Zhang and M. He, *ACS Appl. Mater. Interfaces*, 2015, **7**, 9630–9637.

47 A. Radoń and D. Lukowiec, *CrystEngComm*, 2018, **20**, 7130–7136.

48 S. C. Yan, Z. S. Li and Z. G. Zou, *Langmuir*, 2009, **25**, 10397–10401.

49 C. Zhao, G. Tan, J. Huang, W. Yang, H. Ren and A. Xia, *ACS Appl. Mater. Interfaces*, 2015, **7**, 23949–23957.

50 Y. Deng, L. Tang, C. Feng, G. Zeng, J. Wang, Y. Lu, Y. Liu, J. Yu, S. Chen and Y. Zhou, *ACS Appl. Mater. Interfaces*, 2017, **9**(49), 42816–42828.

51 H. H. Huang, X. P. Ni, G. L. Loy, C. H. Chew, K. L. Tan, F. C. Loh, J. F. Deng and G. Q. Xu, *Langmuir*, 1996, **12**, 909–912.

52 S. He, J. Yao, S. Xie, S. Pang and H. Gao, *Chem. Phys. Lett.*, 2001, **343**, 28–32.

53 G. K. Wertheim, S. B. DiCenzo and D. N. E. Buchanan, *Phys. Rev. B: Condens. Matter Mater. Phys.*, 1986, **33**, 5384–5390.

54 G. K. Wertheim and S. B. DiCenzo, *Phys. Rev. B: Condens. Matter Mater. Phys.*, 1988, **37**, 844–847.

55 F. Dong, Z. Zhao, T. Xiong, Z. Ni, W. Zhang, Y. Sun and W.-K. Ho, *ACS Appl. Mater. Interfaces*, 2013, **5**, 11392–11401.

56 L. Pi, R. Jiang, W. Zhou, H. Zhu, W. Xiao, D. Wang and X. Mao, *Appl. Surf. Sci.*, 2015, **358**, 231–239.

57 J. Zhang, M. Zhang, G. Zhang and X. Wang, *ACS Catal.*, 2012, **2**, 940–948.

58 V. V. Atuchin, E. N. Galashov, O. Y. Khyzhun, A. S. Kozhukhov, L. D. Pokrovsky and V. N. Shlegel, *Cryst. Growth Des.*, 2011, **11**, 2479–2484.

59 W. Yan, X. Liu, S. Hou and X. Wang, *Catal. Sci. Technol.*, 2019, **9**, 1141–1153.

60 X. Bai, L. Wang and Y. Zhu, *ACS Catal.*, 2012, **2**, 2769–2778.

61 T. Ye, W. Huang, L. Zeng, M. Li and J. Shi, *Appl. Catal., B*, 2017, **210**, 141–148.

62 N. K. Veldurthia, N. K. R. Eswar, S. A. Singha and G. Madras, *Catal. Sci. Technol.*, 2018, **8**, 1083–1093.

63 A. Hezam, K. Namratha, Q. A. Drmosh, D. Ponnamma, J. Wang, S. Prasad, M. Ahamed, C. Cheng and K. Byrappa, *ACS Appl. Nano Mater.*, 2020, **3**(1), 138–148.

64 H. Liu, X. Zhao, H. Shen, S. Hao and X. Jiang, *CrystEngComm*, 2021, **23**, 1336–1344.

65 E. Longo, D. P. Volanti, V. M. Longo, L. Gracia, I. C. Nogueira, M. A. P. Almeida, A. N. Pinheiro, M. M. Ferrer, L. S. Cavalcante and J. Andrés, *J. Phys. Chem. C*, 2014, **118**, 1229–1239.

66 M. Li, Q. Meng, S. Li, F. Li, Q. Zhu, B.-N. Kim and J.-G. Li, *Ceram. Int.*, 2019, **45**, 10746–10755.

67 D. W. deQuilettes, S. Koch, S. Burke, R. K. Paranji, A. J. Shropshire, M. E. Ziffer and D. S. Ginger, *ACS Energy Lett.*, 2016, **1**, 438–444.

68 H. A. Atwater and A. Polman, *Nat. Mater.*, 2010, **9**, 205–213.

69 J. H. Lee, J. H. Park, J. S. Kim, D. Y. Lee and K. Cho, *Org. Electron.*, 2009, **10**, 416–420.

70 E. Kymakis, G. D. Spiropoulos, R. Fernandes, G. Kakavelakis, A. G. Kanaras and E. Stratakis, *ACS Photonics*, 2015, **2**, 714–723.

71 A. H. Slavney, T. Hu, A. M. Lindenberg and H. I. Karunadasa, *J. Am. Chem. Soc.*, 2016, **1387**, 2138–2141.

72 E. Greul, M. L. Petrus, A. Binek, P. Docampo and T. Bein, *J. Mater. Chem. A*, 2017, **5**, 19972–19981.

73 W. S. Yang, B.-W. Park, E. H. Jung, N. J. Jeon, Y. C. Kim, D. U. Lee, S. S. Shin, J. Seo, E. K. Kim, J. H. Noh and S. I. Seok, *Science*, 2017, **356**, 1376–1379.

74 L. Zhang, M. Zhou, Z. Zhang, J. Yuan, B. Li, W. Wen and J. Tian, *J. Mater. Chem. A*, 2019, **7**, 22229–22234.

75 L. Li, A. Pandey, D. J. Werder, B. P. Khanal, J. M. Pietryga and V. I. Klimov, *J. Am. Chem. Soc.*, 2011, **133**, 1176–1179.

76 D. W. Abbott and T. Vo-Dinh, *Anal. Chem.*, 1985, **57**, 41–45.

77 C. He, W. Zhu, Y. Xu, T. Chen and X. Qian, *Anal. Chim. Acta*, 2009, **651**, 227–233.

78 G. W. Wu, S. B. He, H. P. Peng, H. H. Deng, A. L. Liu, X. H. Lin, X. H. Xia and W. Chen, *Anal. Chem.*, 2014, **86**, 10955–10960.

79 A. Singh, R. Pasricha and M. Sastry, *Analyst*, 2012, **137**, 3083–3090.

80 V. D. Suryawanshi, L. S. Walekar, A. H. Gore, P. V. Anbhule and G. B. Kolekar, *J. Pharm. Anal.*, 2016, **6**, 56–63.

81 Y. Zhang, Y. H. He, P. P. Cui, X. T. Feng, L. Chen, Y. Z. Yang and X. G. Liu, *RSC Adv.*, 2015, **5**, 40393–40401.

82 Q. Li, M. Zhou, Q. Yang, Q. Wu, J. Shi, A. Gong and M. Yang, *Chem. Mater.*, 2016, **28**, 8221–8227.

83 Y. Tao, K. Yuan, T. Chen, P. Xu, H. Li, R. Chen, C. Zheng, L. Zhang and W. Huang, *Adv. Mater.*, 2014, **26**, 7931–7958.

84 H. Wang, S. Jiang, S. Chen, D. Li, X. Zhang, W. Shao, X. Sun, J. Xie, Z. Zhao, Q. Zhang, Y. Tian and Y. Xie, *Adv. Mater.*, 2016, **28**, 6940–6945.

85 F. Mustafa and S. Andreescu, *RSC Adv.*, 2020, **10**, 19309–19336.

86 M. Davoodi, F. Davar, M. R. Rezayat, M. T. Jafari, M. Bazarganipour and A. E. Shalan, *RSC Adv.*, 2021, **11**, 13245–13255.

87 W. Wu, M. Jia, Z. Wang, W. Zhang, Q. Zhang, G. Liu, Z. Zhang and P. Li, *Microchim. Acta*, 2019, **186**, 97.

88 Y. Yuan, Y. Wu, H. Wang, Y. Tong, X. Sheng, Y. Sun, X. Zhou and Q. Zhou, *J. Hazard. Mater.*, 2020, **386**, 121658.

89 G. M. Sangaonkar, M. P. Desai, T. D. Dongale and K. D. Pawar, *Sci. Rep.*, 2020, **10**, 2037.

90 T. S. Munonde and P. N. Nomngongo, *Sensors*, 2021, **21**, 131.

91 S. Kokilavani, A. Syed, A. M. Thomas, A. M. Elgorban, A. H. Bahkali, N. Marraiki, L. L. Raju, A. Das and S. S. Khan, *J. Mol. Liq.*, 2021, **321**, 114742.

92 N. D. Acha, C. Elosúa, J. M. Corres and F. J. Arregui, *Sensors*, 2019, **19**, 599.